Directly revealing the structure-property correlation in $Na^+ - doped$ cathode materials

Directly revealing the structure-property correlation in Na^+-doped cathode materials

Chao-Fan Li[a,b,†], Liang-Dan Chen[a,†], Liang Wu[a,†], Yao Liu[c], Zhi-Yi Hu[a,b,*], Wen-Jun Cui[b], Wen-Da Dong[a], Xiaolin Liu[d], Wen-Bei Yu [a], Yu Li[a,*], Gustaaf Van Tendeloo[a,b,e], Bao-Lian Su[a,f,*]

[a] State Key Laboratory of Advanced Technology for Materials Synthesis and Processing, Wuhan University of Technology, 122 Luoshi Road, 430070 Wuhan, Hubei, China

[b] Nanostructure Research Centre (NRC), Wuhan University of Technology, 122 Luoshi Road, 430070 Wuhan, Hubei, China

[c] Institute for New Energy Materials and Engineering/College of Materials Science & Engineering, Fuzhou University, Fuzhou 350108, China

[d] State Key Laboratory of Silicate Materials for Architectures, International School of Materials Science and Engineering, Wuhan University of Technology, 122 Luoshi Road, 430070 Wuhan, Hubei, China

[e] Electron Microscopy for Materials Science (EMAT), University of Antwerp, Groenenborgerlaan 171, 2020 Antwerp, Belgium

[f] Laboratory of Inorganic Materials Chemistry (CMI), University of Namur, 61 rue de Bruxelles, B-5000 Namur, Belgium

[†] These authors contribute equally to this work.

[*]Corresponding author. Email: zhiyi.hu@whut.edu.cn, yu.li@whut.edu.cn and bao-lian.su@unamur.be

Abstract

The introduction of Na^+ is considered as an effective way to improve the performance of Ni-rich cathode materials. However, the direct structure-property correlation for Na^+ doped NCM-based cathode materials remain unclear, due to the difficulty of local and accurate structural characterization for light elements such as Li and Na. Moreover, there is the complexity of the modeling for the whole Li ion battery (LIB) system. To tackle the above-mentioned issues, we prepared Na^+-doped $LiNi_{0.6}Co_{0.2}Mn_{0.2}O_2$ (Na-NCM622) material. The crystal structure change and the lattice distortion with picometers precision of the Na^+-doped material is revealed by Cs-corrected scanning transmission electron microscopy (STEM). Density functional theory (DFT) and the recently proposed electrochemical model, i.e., modified Planck-Nernst-Poisson coupled Frumkin-Butler-Volmer (MPNP-FBV), has been applied to reveal correlations between the activation energy and the charge transfer resistance at multiscale. It is shown that Na^+ doping can reduce the activation energy barrier from ΔG = 1.10 eV to 1.05 eV, resulting in a reduction of the interfacial resistance from 297 Ω to 134 Ω. Consequently, the Na-NCM622 cathode delivers a superior capacity retention of 90.8% (159 $mAh.g^{-1}$) after 100 cycles compared to the pristine NCM622 (67.5%, 108 $mAh.\ g^{-1}$). Our results demonstrate that the kinetics of Li^+ diffusion and the electrochemical reaction can be enhanced by Na^+ doping the cathode material.

Keywords: $LiNi_{0.6}Mn_{0.2}Co_{0.2}O_2$; Na^+-doping; Transmission electron microscopy; Migration energy barrier, Charge transfer resistance

1. Introduction

Over the past decades, Ni-rich cathode materials, e.g., $LiNi_{0.6}Co_{0.2}Mn_{0.2}O_2$ (NCM622) and $LiNi_{0.8}Co_{0.1}Mn_{0.1}O_2$ (NCM811), have attracted great attention in terms of high specific energy density, relatively low cost, and superior cell performance [1-3]. Nevertheless, the rapid capacity decline and structural instability are inevitable challenges for the development of Ni-rich layered cathode materials [4-12]. In this regard, cationic doping has been identified as a promising option to simultaneously improve the electrochemical performance and structural stability [13-15]. As an alkaline metallic cation, sodium (Na) has a large ionic radius and similar chemical properties as lithium (Li); Moreover, it is widely used to improve the performance of NCM-based cathode materials. However, the direct and essential structure-property correlation in these Na^+ doping NCM-based cathode materials is still unclear. On the one hand, the local and accurate structural characterization is difficult for light elements such as Li and Na. On the other hand, the whole system of a Li ion battery (LIB) is complicated, so that practical factors, such as interfacial effects, electrolyte and the different diffusivity of Li^+ in the cathode or electrolyte, are easily ignored in modeling the structure-property correlation via calculation methods.

To study of fine microstructure, (scanning) transmission electron microscopy ((S)TEM) and X-ray diffraction (XRD) are usually employed to investigate Na^+-doped cathode materials in order to explain the superior electrochemical performance of LIBs [16, 17]. The introduction of Na^+ into layered cathode induces a low-angle shift of the (003) and (104) interplanar peaks in the XRD characterization [18], while direct evidence is generally demonstrated by (S)TEM [15, 17]. It is mostly accepted that the Na ions will occupy the Li^+ positions [16, 19]. As Li and Na are light elements, it is hard to reveal the local information by XRD, but also in electron microscopy it is not straightforward as lighter elements have less scattering power during the interaction with the electron beam. However, thanks to the state-of-the-art (S)TEM techniques, and aberration corrected imaging [20, 21], picometer precision can be obtained [22] and the

fine structure of Na^+-doped cathode materials analyzed.

Density functional theory (DFT) calculation methods are generally used to illuminate the correlation of the fine structure and the electrochemical performance of NCM-based cathode materials. Based on the DFT analysis, an enlarged layer distance can reduce the activation energy barrier, improving the Li mobility in the layered cathode material [23]. But how the activation energy influences the electrochemical performance is rarely discussed. This is because DFT calculations mainly focus on atomic-scale studies, and thus explain the performance based on the intrinsic properties of the material, e. g. the atomic structure and the activation energy. However, they ignore the overall impedance of the battery and therefore there is an urgent need to directly calculate the interface impedance of Na^+-doped NCM materials in LIBs on a multi-scale.

To tackle these issues, we prepared Na^+-doped $LiNi_{0.6}Co_{0.2}Mn_{0.2}O_2$ (Na-NCM622) cathode materials via a hydroxide co-precipitation process and characterized the crystal structure with picometer precision by Cs-corrected scanning transmission electron microscopy (STEM) equipped with RevSTEM drift correction [22]. Direct observations confirm that the doped Na^+ replace the Li, thereby inducing local lattice distortions in the cathode material. In order to investigate the structure-property correlation and the improved electrochemical performance of Na-NCM622, DFT calculations have been used to clarify the lower activation energy barrier of Li^+ and the enhanced kinetics of Li^+ diffusion. To further understand the correlation between the activation energy and the electrochemical performance, an advanced electrochemical model and the corresponding equivalent circuit model for LIBs impedance calculations has been employed, based on our previous work [24]. Using this electrochemical model, the charge transfer resistance of Na-NCM622 and NCM622 can be calculated as 134 Ω and 297 Ω respectively; this decrease can be ascribed to the fast reaction kinetics of Li^+ via Na^+ doping. With the combination of advanced structural characterization and multi-scale calculations we can gain direct insight into the functioning of Na-NCM622 cathode materials.

The correlation between the fine microstructure and the battery performance is further discussed from the perspective of theoretical electrochemistry.

2. Experimental section

2.1 Synthesis of NCM622 and Na-NCM622 nanoparticles

Nowadays, various advanced strategies of electrode fabrication, including templating method [25], chemical self-assembly [26], 3D printing method [27, 28] and so on, have been reported for high energy density of lithium battery. Herein, we used the hydroxide co-precipitation method to obtain the electrode samples and the $Ni_{0.6}Co_{0.2}Mn_{0.2}(OH)_2$ precursor was prepared from $NiSO_4 \cdot 6H_2O$, $CoSO_4 \cdot 7H_2O$, $MnSO_4 \cdot H_2O$, NaOH, and NH_4OH. An aqueous solution (Ni: Co: Mn = 6: 2: 2 in molar ratio, 2 mol L^{-1}) of transition-metal sulfates was added to a continuously stirred reactor under N_2 atmosphere. 4 mol·L^{-1} NaOH (aq.) and 10 mol·L^{-1} NH_4OH (aq.) were also added to the reactor, and the pH was kept at 11.5. Thereafter, the dried hydroxide precursor and 5% excess $LiOH \cdot H_2O$ were mixed and calcinated at 750 ˚C for 12 h in air. The obtained material is labeled as NCM622. To obtain Na^+-doped NCM622 materials, the precursor was mixed with $LiOH \cdot H_2O$ and CH_3COONa. Thereafter, the mixture was calcinated under the same conditions as $LiNi_{0.6}Co_{0.2}Mn_{0.2}O_2$, and the as-prepared material is denoted as Na-NCM622.

2.2 Structural Characterization

An inductively coupled plasma optical emission spectrometer (ICP-OES) (OPIMA 8300, Perkin Elmer) was used to determine the chemical composition of as-prepared cathode materials. Crystal structure and phase composition were determined by X-ray diffraction (XRD) using a Bruker diffractometer with Cu-Kα radiation. The morphology and the elemental distribution of the samples were characterized by a Hitachi S-4800 field emission scanning electron microscope (SEM) equipped with an energy dispersive X-ray spectrometer (EDS). X-

ray photoelectron spectroscopy (XPS) was carried out on a VG Multilab 2000 to determine the chemical valence states of Ni, Co, Mn, Na. Atomic resolution scanning transmission electron microscopy (STEM) was performed on a Thermo Fisher Themis microscope fitted with aberration correctors for both the probe forming and the imaging lens, at 300kV. All the atomic resolution images with picometer precision were drift corrected by the RevSTEM program[22].

2.3 Electrochemical Characterization

Positive electrodes were obtained by coating a slurry of the active powder, super-P and polyvinylidene fluoride with a ratio of 8:1:1 (wt%). Then, the slurry was pasted on an Al foil and dried in the oven at 120 ℃ for 12h. The electrochemical properties of the cathode materials were tested by assembling coin-type (CR2025) cells in an argon filled glove box. The electrolyte was composed of 1.0 M $LiPF_6$ in ethylene carbonate (EC), dimethyl carbonate (DMC) and ethyl methyl carbonate (EMC) (1:1:1 in wt%). The cycle performance of the cell was carried out on a LAND CT2001A battery machine with a voltage ranging from 2.7~4.3 V. Cyclic voltammetry (CV) was performed on a CHI 660D electrochemical workstation at a scan rate of 0.2 mV s^{-1} up to 4.3 V (vs Li/Li^+). The Autolab PG302N was utilized to obtain the electrochemical impedance spectroscopy (EIS) results in the frequency range from 10 mHz to 100 kHz.

2.4 Density functional theory

The DMol3 code in Material Studio (version 2018) of Accelrys Inc was used for the DFT calculations. The Perdew-Burke-Ernzerhof (PBE) generalized gradient approximation (GGA) was used to examine the electronic exchange-correlation function for the electron interactions. According to the DFT-D correction calculated by Grimme, the van der Waals interactions could be explained. For the ultrasoft plane-wave basis, 500 eV was defined as the energy cutoff value. The supercell was sampled using the Brillouin zone with a regular mesh of 1×1×1 k-points. The

convergence energy for the electronic self-consistency loop was 10^{-5} eV, and the maximum force tolerance of structural optimization was set to 0.05 eV/Å.

2.5 Electrochemical model

To investigate the correlation between atomic structure and the electrochemical performance, our recently proposed, modified Planck-Nernst-Poisson coupled Frumkin-Butler-Volmer (MPNP-FBV) model was applied [24, 29, 30]. The governing equations are given as:

$$\frac{\partial c_i}{\partial t} = \frac{D_i}{1-\tilde{c}_i}\nabla^2 c_i + z_i \frac{FD_i}{RT}\nabla \cdot (c_i \nabla \Phi) \quad (1)$$

$$\nabla^2 \Phi = -\frac{F}{\varepsilon_0 \varepsilon_i}\sum z_i c_i \quad (2)$$

The concentration of Li^+ and the electrostatic potential are denoted by c_i and Φ, and the subscript "i" indicates the electrolyte and the cathode, respectively. D_i represents the diffusion coefficient of Li^+, which is closely related to the atomic structure of the materials. ε_0 and ε_i are the permittivity, F denotes the Faraday constant, R is the gas constant, T indicates the temperature, and z_i is the valence.

From an electrochemical point of view, the reaction kinetics at the interface plays an important role in the battery performance and is expressed as $Li + V_{Li^+} \rightleftharpoons Li^+ + V_{Li} + e^-$. To get closer to reality, the vacancy effect has been included and is denoted by V_{Li} (V_{Li^+}). The lithiation/delithiation process can reach an intrinsic dynamic equilibrium state without external perturbation and the charge transfer resistance of the battery can be determined under this circumstance. The corresponding equation is expressed as

$$R_{ct} = \frac{RT}{F^2 A (K_o')^{1-\beta} (K_r')^{\beta} (c_o^{eq})^{1-\beta} (c_{max}-c_r^{eq})^{1-\beta} (c_r^{eq})^{\beta} (c_{max}-c_o^{eq})^{\beta}} \quad (3)$$

Where c_{max} denotes the maximum concentration of materials, c_r and c_o are the interface concentrations associated with the reaction, and the superscript "eq" denotes the intrinsic equilibrium state. K_o' and K_r' are the material properties and are given by

$$K'_o = K_o \exp\left(-\frac{F\Delta G_o^{\Theta}}{RT}\right) \qquad K'_r = K_r \exp\left(-\frac{F\Delta G_r^{\Theta}}{RT}\right) \tag{4}$$

K_o and K_r are depending on the temperature, ΔG_i^{Θ} is the standard activation energy barrier of the material, which is related to the atomic structure. It can be clearly seen that the atomic structure plays an important role in the activation energy of materials, thereby determining the interfacial impedance and the electrochemical performance. To gain insight into the influence of the Na^+doping, the activation energy, i.e., ΔG_i^{Θ}, is determined by the DFT calculations in this work. K_o and K_r depend on the temperature and are called the reaction rate, β is usually given as 0.5, and A is the cross-section area. Numerical simulations were performed using the finite element method (FEM) in the MOOSE framework with 5000 second-order elements.

3. Results and discussion

3.1 Characterization of NCM622 and Na-NCM622

The synthesis of the as-prepared Na^+-doped materials is illustrated in Fig. S1a, and Fig. S1b shows that NCM622 and Na-NCM622 cathodes have a spherical morphology. No obvious difference is observed in the surface morphology between both samples, indicating that the doping by Na^+ will not alter the morphology, as shown in Fig. S1c-d. The EDS elemental maps further confirm that Ni, Co, Mn and Na are homogeneously distributed inside the material. Table. S1 illustrates the chemical composition of the as-prepared materials, the results show that the relative atomic ratio is close to the designed value, i.e., Ni: Co: Mn=6:2:2.

Fig. 1a schematically shows the Na^+ doping, replacing the Li sites and leading to an enlarged layer distance and lattice distortion. Fig. 1b illustrates the XRD patterns of NCM622 and Na-NCM622, respectively. The characteristic peaks indicate that the as-prepared materials have a high degree of crystallinity, and can be indexed as the hexagonal α-$NaFeO_2$ layered structure with space group $R\bar{3}m$. The distinct separation of the (108)/(110) and (006)/(102) peaks suggests that the doping Na^+ plays a negligible influence on the crystalline layer structure

[31]. However, the peaks of (003) and (104) shift toward the lower angle region, indicating that the Na^+ doping induces an expansion of the interlayer spacing; this clearly favors the diffusion coefficient [32]. The XRD patterns are analyzed by Rietveld refinement (Fig. S2) and the refined structural parameters are shown in Table 1. The c-lattice value increases from 14.2403 to 14.2615 Å, obviously showing the lattice expansion of the Na-NCM622 material. The calculated XRD results show that the concentration of Ni^{2+} is approximately 1.18% in the Li layer, which is much lower than that of the pristine sample, i.e., 2.19%. It is accepted that a well-organized layer structure can be formed when the intensity ratio I_{003}/I_{104} is larger than 1.2 [33]; In our case, the I_{003}/I_{104} ratio of Na-NCM622 and NCM622 is 1.78 and 1.52, respectively. These results indicate that the as-prepared materials have a good layered structure.

In order to analyze the surface element oxidation state after Na^+-doping, XPS measurements were performed and the results are shown in Figs. 1c-h. As can be seen in Fig. 1c, the Na 1s peak is only located at 1071 eV with a strong intensity, indicating that Na^+ was successfully doped into the sample. The characteristic peaks centered at 872.5 eV and 854.7 eV represent Ni 2p 1/2 and Ni 2p 3/2, respectively (Fig.1d). The spin-energy difference is 17.8 eV, thus predicating that most of the Ni has a valence of +2 [34]. The well fitted peaks centered at 795 and 780 eV (Fig. 1e) can be assigned to Co 2p 1/2 and Co 2p 3/2, further demonstrating that the valence state of Co is +3 [35]. The high-resolution Mn 2p spectrum is shown in Fig. 1f. The peaks located at 654 eV and 642 eV correspond to Mn 2p 1/2 and 2p 3/2, indicating the existence of a mainly 4+ valence state [36]. There is no peak shift in the XPS results, implying that the valence states of Ni, Co, and Mn remain stable after Na^+-doping. As well, the local oxidation states of Ni, Co and Mn can be verified from electron energy loss spectroscopy (EELS) [37, 38], where no chemical shift can be observed both on the surface and in the bulk of the two samples (Fig. S3). With the introduction of Na^+, the spectrum of O 1s, centered at 531.3 eV, is reduced while the peak at 529.5 eV increases. It indicates that the surface oxygen species, i.e., Li_2CO_3 and LiOH, can be alleviated by the doping with Na^+. In Fig. 1h, the weak peak located

at 289.8 eV can be assigned to the decreased amount of $LiCO_3$. The XPS results of O 1s and C 1s indicate the improved integrity of the layered structure, which is favorable for the extraction and intercalation process of Li^+.

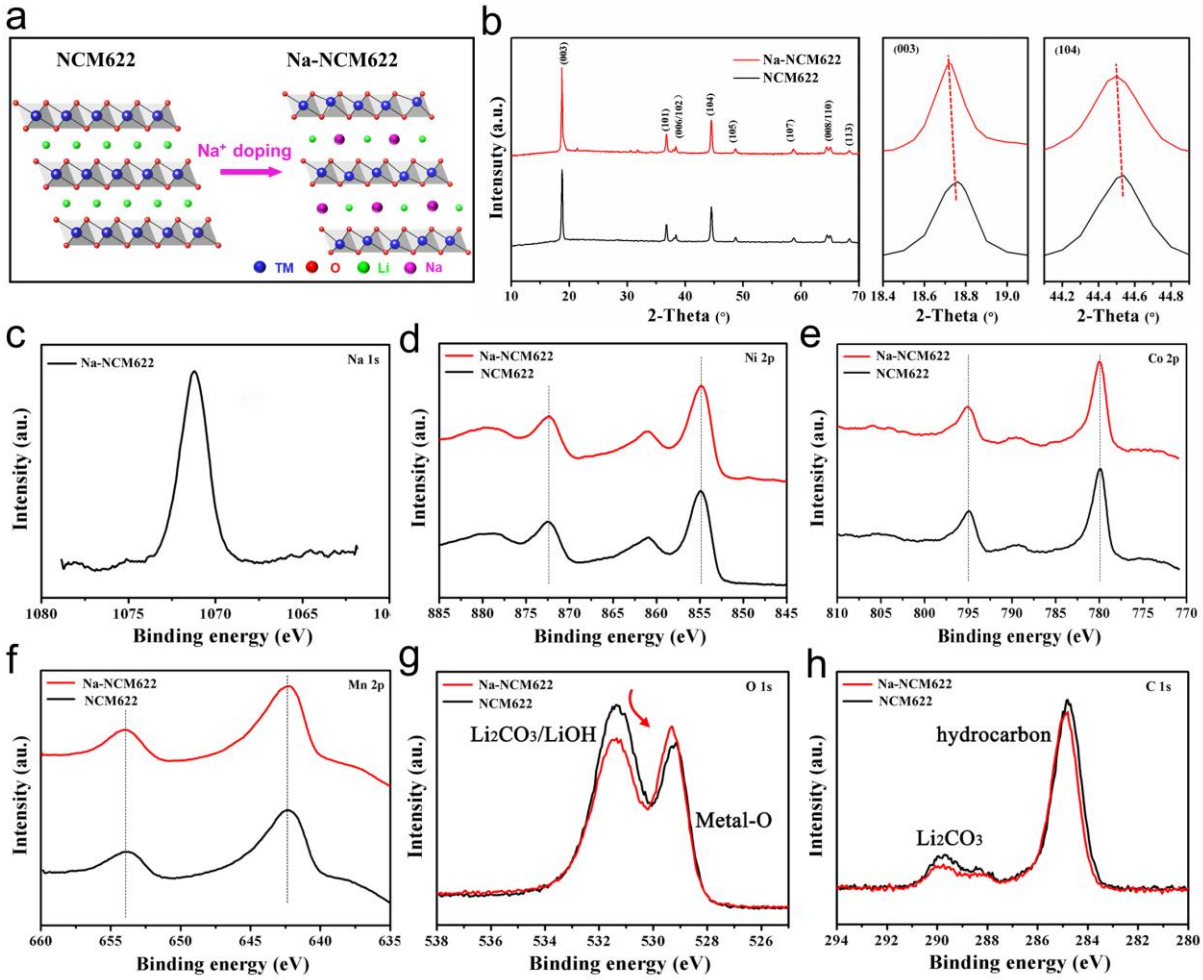

Fig. 1. (a) XRD patterns of NCM622 and Na-NCM622; (b) Schematic illustration of the crystal structure of the cathode materials; XPS spectra of (c) sodium (Na), (d) nickel (Ni), (e) cobalt (Co), (f) manganese (Mn), (g) oxygen (O), (h) carbon (C), in the samples.

Table 1. Refined structural parameters of the NCM622 and Na-NCM622.

Materials	a (Å)	c (Å)	Ni/Li (%)	I_{003}/I_{104}	Rwp (%)	Rp (%)
NCM622	2.8756	14.2403	2.19	1.78	2.78	2.68
Na-NCM622	2.8701	14.2615	1.18	1.52	2.48	2.67

Cs-corrected and drift corrected scanning transmission electron microscopy (STEM) was performed to investigate the precise location of the doped Na ions at an atomic scale. For

comparison, the pristine NCM622 sample was also analyzed by high angle annular dark field scanning transmission electron microscopy (HAADF-STEM). Figs. 2a and 2d present the typical layered structure of NCM622 and Na-NCM622 along the [010] zone axis. The bright dots represent the atomic columns of the transition metal (TM) layer, whereas Li atoms are hardly visible. This because the HAADF-STEM contrast is roughly proportional to the atomic number squared and Li as well as Na have a low atomic number [39]. Therefore, in order to study the influence of the Na^+ doping, the TM (Ni, Co, Mn) positions are registered with picometer precision in the HAADF-STEM images; this with the help of drift corrected by RevSTEM [22] and indicated by CalAtom [40]. After the introduction of Na^+, the lattice distortion of the area indicated by green box in Figs. 2a and 2d can be clearly observed in Fig. 2b and 2e, where the twisted quadrilateral structures (indicated by the orange arrows) can be seen directly.

Fig. 2c and 2f are the corresponding electron scattering intensity maps of NCM622 and Na-NCM622. The marked atomic columns (red arrows) are brighter in Na-NCM622 (Fig.2 f) compared to NCM622 which almost have no contrast (Fig. 2c), suggesting that heavier atoms occupy the Li-sites. The corresponding intensity line profile (Fig. 2i) of Na-NCM622 also reveals dots with a weak intensity at some atomic columns in the Li layers (indicated by red arrows in Figs. 2f and 2i). Such dots with weak intensity are absent in the intensity map of the pristine NCM622 (Fig. 2c) as well as in the line profile (black curve in Fig. 2i). The fact that the intensity at the Li position is low compared to the intensity of the TM columns again points towards the occupation of Na on the Li sites. Fig. 2h demonstrates the local layer separation between two neighboring TM slabs, i.e., the Li interlayer spacing. The distance is uniform and approximately equal to 490 ±7 pm for the NCM622 sample. With the introduction of Na^+, the interplanar spacing increases and strongly fluctuates between 500 and even 540 pm. This large fluctuation of the layer spacing is caused by a variation of the lattice distortion, which itself is related to the local Na doping [41]. Fig. S4c and d also show that doping Na^+ partially occupies

the site of Li, resulting in a local extension of the interlayer spacing.

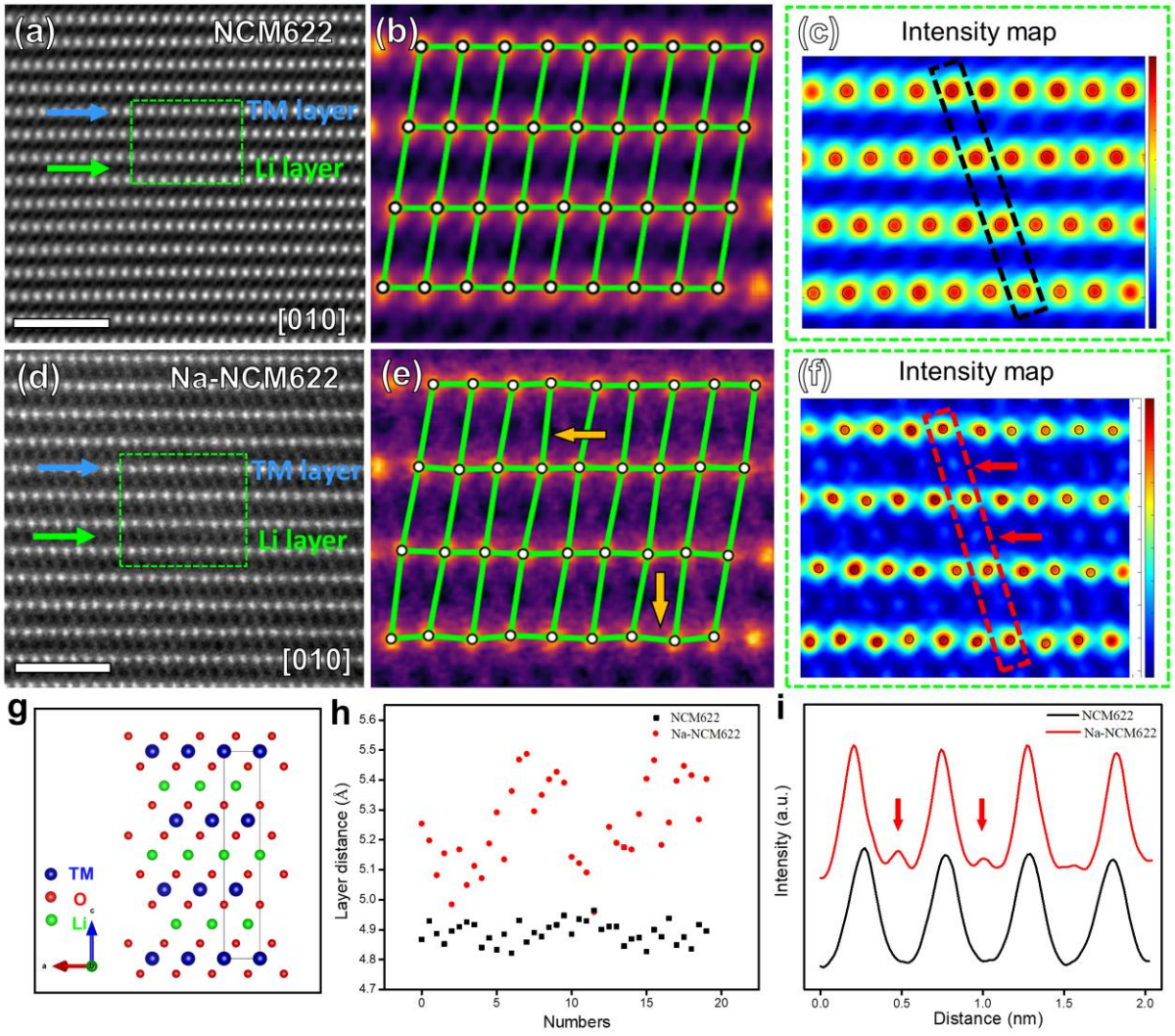

Fig. 2. (a) Atomic HAADF-STEM image of pristine NCM622; (b-c) Corresponding marked map and intensity map of the area indicated by the green box in (a); (d) Atomic HAADF-STEM image of Na-NCM622; (e-f) Corresponding marked map and intensity map of the area indicated by the green box in (d); (g) Crystal structure of layered structure along [010] zone axis: Transition metals (blue), Oxygen (red) and Lithium (green); (h) Dot plot of the calculated local layer separation; (i) Intensity line profiles of the dark and red rectangles in (c), (f).

3.2 Electrochemcial performance of LIBs

The electrochemical performance of Na-NCM622 and NCM622 cathodes was evaluated in coin-cells with lithium foil as counter electrode. Fig. 3a displays the CV curves in the voltage range from 2.7 V to 4.3 V in the first cycle. The two sharp redox peaks are ascribed to the redox reaction of Ni^{2+}/Ni^{4+} [42]. The potential gap between cathodic peak and anodic peak is 0.27 V

for pristine Na-NMC622, which is lower than that for NMC (0.32 V), suggesting that Na^+ doping can effectively reduce the potential polarization during the charge-discharge process. This result is further confirmed by the initial charge-discharge curves at 0.1C as shown in Fig. 3b. The Na-NCM622 cathode shows a small potential polarization and delivers initial charge and discharge capacities of 192.8 and 179 mAh g^{-1}, respectively. And the initial coulombic efficiency is 84.40% for Na-NCM622 cathode. By contrast, the NCM622 cathode delivers charge and discharge capacities of 181.5 and 168 mAh g^{-1} with a coulombic efficiency of 80.77%. The improvement of discharge capacity and coulombic efficiency can be ascribed to the enhanced lattice stability and fast Li^+ diffusion induced by the Na^+ doping, favoring more Li ions extraction/insertion under the same cutoff voltage [43].

Fig. 3c presents the rate performance of the prepared cathodes with a step-increasing current density of 0.1C, 0.2C, 0.5C, 1C, 2C and 5C, and then restored to 0.2C. The Na-NCM622 cathode delivers a capacity of 192.8, 171.3, 152.6, 141.5, 128.6 and 105.8 mAh.g^{-1} at 0.1, 0.2, 0.5, 1, 2 and 5C. The specific capacities of the Na-NCM622 cathode at each current density are all higher than that of the pristine NCM622 cathode, demonstrating that the enlarged layer space caused by Na^+ doping allows the fast Li^+ diffusion and promotes Li^+ migration kinetics [44, 45]. The discharge voltage curves in Fig. 3d show the reduced discharge capacities for both Na-NCM622 and NCM622 cathodes with increasing current density due to the electrochemical polarization. In addition, when the electrodes are charged to 4.0 V, the discharge capacities at low current density are identical for both NCM622 and Na-NCM622, delivering 40 mAh g^{-1} at 0.1 C, 30 mAh g^{-1} at 0.2 C, 25 mAh g^{-1} at 0.5 C, and 19 mAh g^{-1} at 1 C. However, the discharge capacities are obviously different at 2 C, which are 9 and 15 mAh g^{-1} for NCM622 and Na-NCM622, respectively. In particular, at a higher discharge current density of 5 C, the Na-NCM622 cathode delivers a higher discharge capacity (8 mAh g^{-1}) than the pristine NCM622 cathode (0 mAh g^{-1}) at the same potential (Fig. S5). These results further indicate that Na^+

doping can effectively lower the potential polarization of Ni-rich oxide cathodes during discharge, especially for high discharge current.

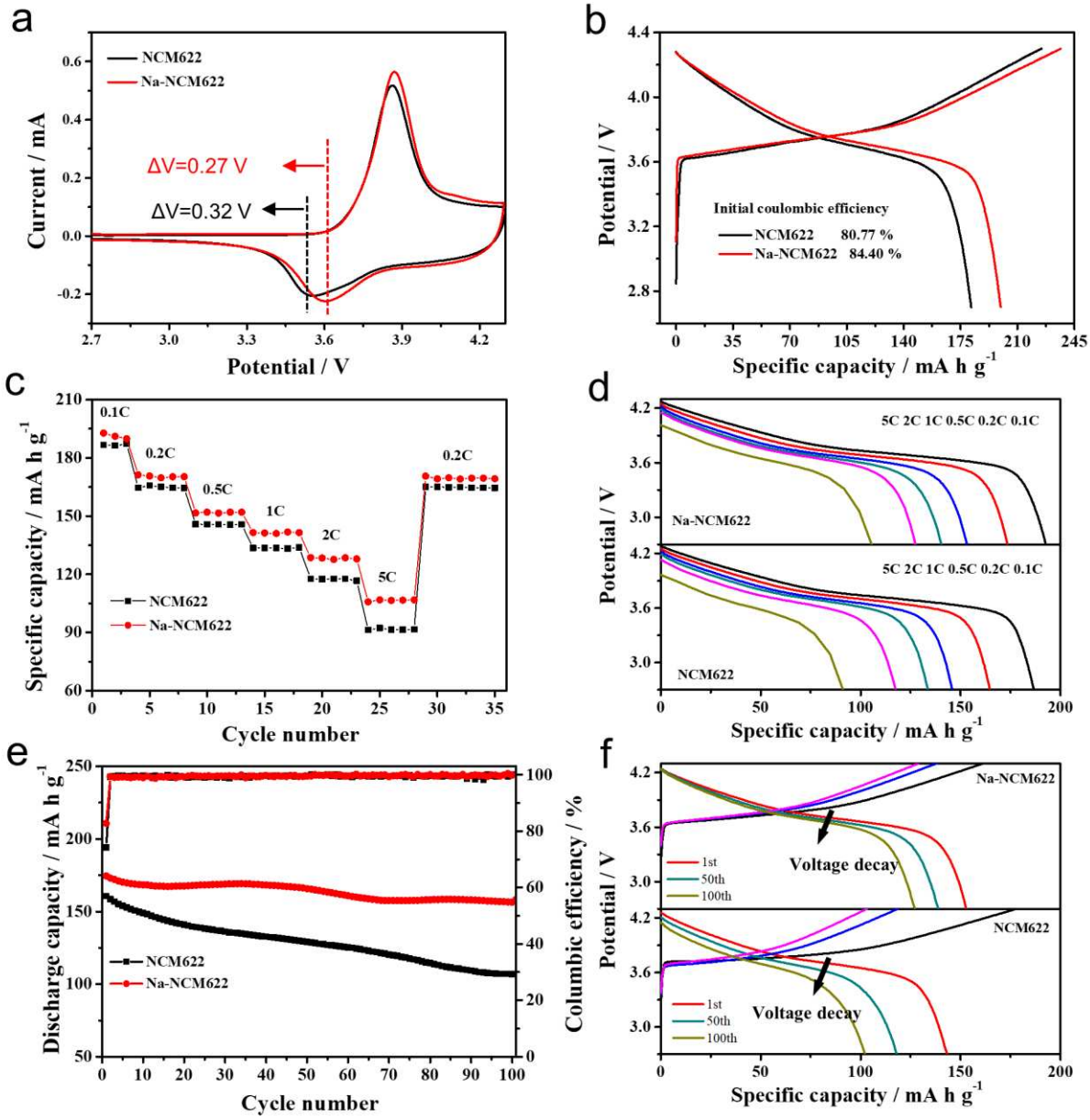

Fig. 3. (a) CV curves and (b) the initial charge/discharge curves of NCM622 and Na-NCM622 cathodes; (c) Rate capability of the cathodes at different C-rates in the range 0.1-5 C; (d) Discharge curves of the cathodes at various rates; (e) Cycling performance of the cathodes at 0.2 C; (f) 1st, 50th, 100th charge-discharge voltage curves at 0.5C.

Fig. 3e presents the cycling performance of NCM622 and Na-NCM622 cathodes at a current density of 0.2 C. The Na-NCM622 cathode shows an initial discharge specific capacity of 175mAh.g^{-1} and a high-capacity retention of 90.8% after 100 cycles. On the other hand, the pristine NCM622 cathode exhibits an initial capacity of 160 mAh.g^{-1} and rapidly fades to 108

mAh.g^{-1} with a lower retention rate of 67.5%. The superior cycling performance may be attributed to a Na^+ pinning effect within a stable layered structure [15]. Table S2 compares the cycling performance with other published NCM622 cathodes. It clearly shows that the as-prepared Na-NCM622 cathode demonstrates a superior cycling stability.

Fig. 3f shows the charge-discharge voltage curves of the 1st, 50th and 100th cycle at 0.5 C. The discharge potential of the undoped pristine NCM622 cathode exhibits a sharp downward shift upon cycling. In contrast, the decay of discharge potential for Na-NMC622 is significantly suppressed over 100 cycles (indicated by the black arrows), suggesting the significant effect of Na^+ doping on suppressing the voltage decay.

The diffusion coefficients of Li^+ in NCM622 and Na-NCM622 cathodes were deduced from the CV curves with a scan rate ranging from 0.2 to 0.5 mV s^{-1} (Figs. 4a-b). The diffusion coefficient can be calculated by the Randles-Sevcik equation and is expressed as [46, 47]

$$I_P = 2.69 \times 10^5 \times n^{\frac{3}{2}} \times A \times D^{\frac{1}{2}} \times C_0 \times v^{\frac{1}{2}} \qquad (1)$$

where n represents the number of electrons per redox reaction, A is the electroactive area, D denotes the diffusion coefficient, and C_0 is the initial concentration of Li^+. The peak current Ip is proportional to the CV scan rates ($v^{1/2}$), and the results are shown in Fig. 4c. Based on Eq. (1), the diffusion coefficients of Li^+ in NCM622 at oxidation and reduction peaks are 1.30×10^{-12} and 3.18×10^{-13}, whereas the diffusivities of Na-NCM622 are 1.82×10^{-12} and 4.71×10^{-13}, respectively. The improved Li^+ diffusion coefficients are clearly related to the enlarged interlayer spacing that favors the extraction/insertion process.

Electrochemical impedance spectroscopy (EIS) measurements were carried out to investigate the electrochemical performance. Fig. 4d shows the Nyquist impedance plots of the charged battery in the frequency range from 10 mHz to 100 kHz. To deepen the understanding, the corresponding equivalent circuit model is also presented here. Generally, the first semicircle in the high-frequency region (R_{sei}) corresponds to effects related with the solid electrolyte interface (SEI) [48, 49]. The second semicircle is attributed to the interface resistance.

Furthermore, the diameter of the semicircle is equal to the charge transfer resistance (R_{ct}) at the electrode/electrolyte interface, which is the kinetically controlled region [50]. The sloping line at low frequencies denotes the Warburg impedance (W_1) associated with the Li^+ diffusion. According to the equivalent circuit model, the battery impedance can be obtained and is listed in Table 2. The charge transfer resistance R_{ct} values of Na-NCM622 and NCM622 are 131.2 and 172.1 Ω at the 10th cycle, respectively. Moreover, the resistances due to the solid electrolyte interface are 35.8 and 47.9 Ω. After 50 cycles, the charge transfer resistances increase to 190 and 233 Ω, and the corresponding SEI impedances are 134 and 246 Ω. It turns out that with the introduction of Na^+, the enlarged layer distance and lattice distortion lead to a lower activation energy barrier, thereby reducing the charge transfer resistance and improving the electrochemical performance.

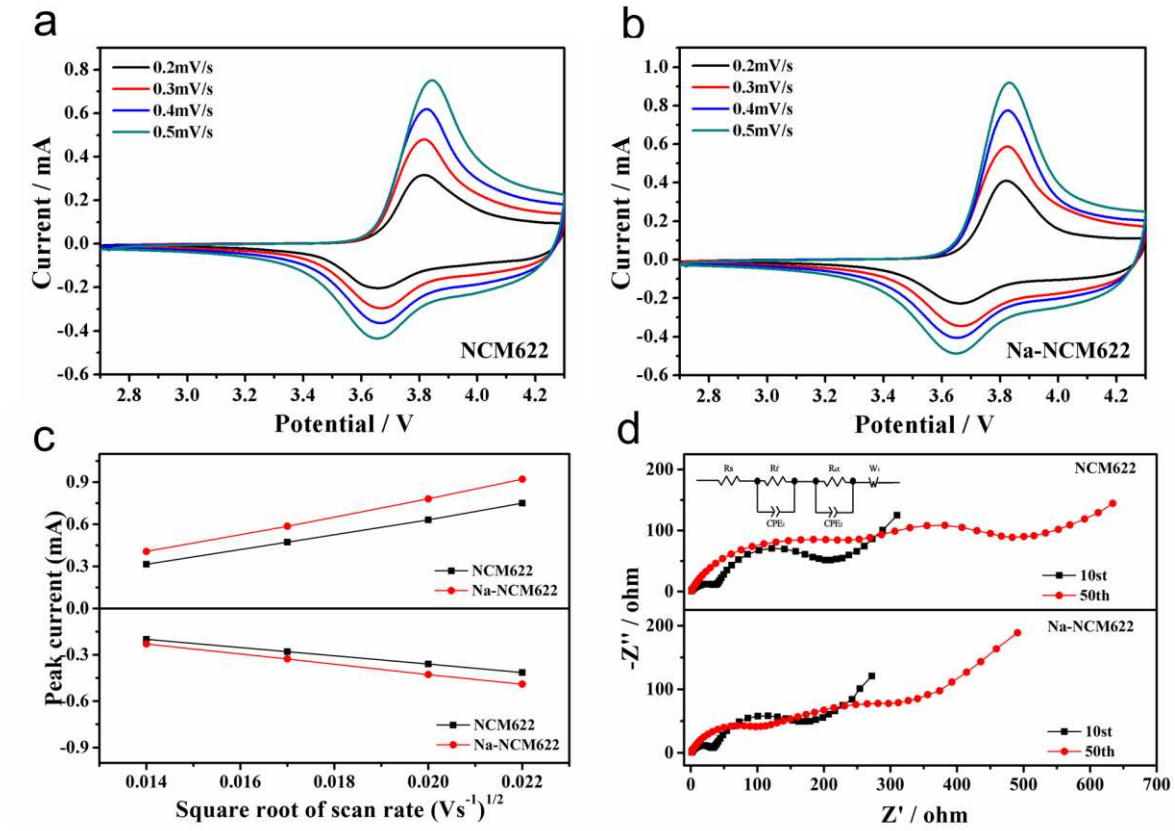

Fig. 4. CV curves of (a) NCM622, (b) Na-NCM622 and (c) Relationship of the peak current (Ip) and the square root of the scan rate ($v^{1/2}$); (d) Nyquist plots of cathodes; as insert, the equivalent circuits used to fit the experimental data.

Table 2. The Impedance parameters of equivalent circuit.

Cycle Number	10st cycle				50st cycle			
	R_s	R_f	R_{ct}	R_{f+ct}	R_s	R_f	R_{ct}	R_{f+ct}
NCM622	2.55	47.9	172.1	190	2.84	246	233	479
Na-NCM622	2.76	35.8	131.2	167	2.96	134	190	324

3.3 DFT calculations

First-principal calculations have been conducted to calculate the activation energy barrier of Li^+ in the as-prepared materials. Owing to the migration mechanism, there exist two different ways for Li^+ transfer to the adjacent site [51]. The first pathway is through the space between two adjacent oxygen ions, known as the oxygen dumbbell hop (ODH) (Fig. 5a). The other is through the tetrahedral position in the middle of the path, considered as the tetrahedral site hop (TSH) (Fig. 5b). At the early stage of delithiation, the migration of Li^+ follows the ODH pathway because of there is no requirement of Li vacancies for Li^+ diffusion. Therefore, we studied the Li^+ activation energy barrier based on the ODH mechanism [52], and the calculated migration pathway can be seen in Fig. S6. Fig.5c shows that the Li^+ activation energy of Na-NCM622 is 1.05 eV, which is slightly smaller than that of NCM622. The energy of the O 1s orbital also shifts to the right with the introduction of Na^+, as illustrated in Fig. 5d. The DFT calculation results show that doping Na^+ can reduce the activation energy of materials, thereby improving the battery performance by enhancing the kinetics of Li^+ diffusion. The calculated activation energies can be involved in the electrochemical model, as described in the following section.

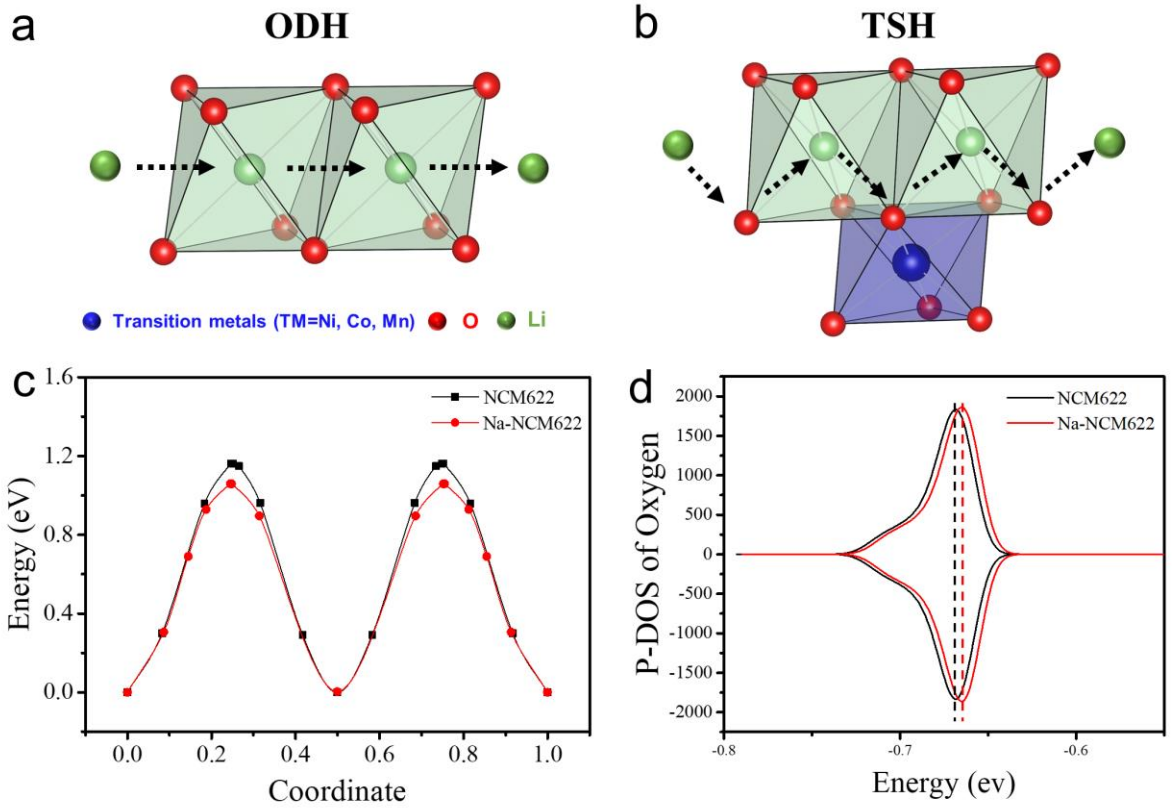

Fig. 5. (a) The first path for Li^+ migration to an adjacent location (ODH); (b) The second path for Li^+ migration to an adjacent location (TSH); (c) Li^+ migration activation barrier of NCM622 and Na-NCM622; (d) O1s state density diagram of the cathode materials.

3.4 Charge transfer resistance calculations

The above-mentioned results demonstrate that the Na-NCM622 cathode reaches a superior electrochemical performance, and the improvement is ascribed to the Na^+ doping with a lower activation energy. In order to link the activation energy and charge transfer resistance, we performed an in-depth study using multi-scale calculations combining the MPNP-FBV model and the DFT results. As shown in Equations (3) and (4), the activation energy, i.e., ΔG_i^{Θ}, plays an important role in the charge transfer resistance that is associated with the kinetics of the electrochemical reaction. The activation energy barriers of Li^+ migration in Na-NCM622 and NCM622, as identified by the DFT calculations in section 3.3, are around 1.05 and 1.10 eV. According to the previous work [53], the activation energy for the diffusion of Li^+ in $LiPF_6$-PC is 0.15 eV (14 kJ/mol). The diffusion coefficients of Li^+ in Na-NCM622 and NCM622 are

derived from Fig. 4c and are 4.71×10^{-13} and 3.2×10^{-13} m^2s^{-1}, respectively. More parameters used in the MPNP-FBV model are shown in Table 3.

Table 3. Parameters used in the MPNP-FBV model.

Parameter	Unit	Value	Description
L_e	nm	30	Thickness of the electrolyte
L_c	nm	30	Thickness of the cathode
λ_s	nm	0.6	Thickness of the Stern layer
D_e	$m^2\ s^{-1}$	4×10^{-11}	Diffusivity of Li^+ in the electrolyte
D_c	$m^2\ s^{-1}$	$3.2\times10^{-13}/4.7\times10^{-13}$	Diffusivity of Li^+ in the cathode
ΔG_e^{Θ}	eV	0.15	Activation energy barrier of the electrolyte
ΔG_c^{Θ}	eV	1.10/1.05	Activation energy barrier of the cathode
ε_e	-	8	Relative permittivity of the electrolyte
ε_c	-	20	Relative permittivity of the cathode
c_e	mol m^{-3}	7×10^3	Initial concentration of the electrolyte
c_c	mol m^{-3}	1×10^3	Initial concentration of the cathode
K_i	$m^4\ mol^{-1}\ s^{-1}$	0.1	Reaction rate
A	m^2	2.3×10^{-4}	Geometrical surface

Fig. 6a shows a schematic NCM-based battery. To focus on the interface behavior and the charge transfer resistance, the electrolyte and the cathode thicknesses are selected as $L_e = L_c =$ 30 nm. Moreover, the active energy barrier ΔG_c^{Θ} of the pristine NCM622 cathode is 1.10 eV. With the introduction of Na^+, the activation energy is reduced to $\Delta G_c^{\Theta} = 1.05$ eV. Relying on the MPNP-FBV model and the activation energy calculated by DFT, the concentration distribution of Li^+ at the intrinsic equilibrium state is shown in Fig. 6b. Clearly more Li^+ accumulates at the interface of NCM622 cell compared to Na-NCM622, forming a thicker space charge layer. Thicker space charge layers lead to a larger interfacial impedance, e.g., the charge transfer resistance and the space charge layer capacitance, which are detrimental to the electrochemical performance. Based on the interface concentrations and Equation (3), the

charge transfer resistances of Na-NCM622 and NCM622 are calculated to be R_{ct} = 134 Ω and R_{ct} = 297 Ω for these two cases. Although the calculated and experimental values are different, it still reveals the correlation between the atomic structure and the electrochemical performance. The enlarged layer distance and lattice distortion are formed after Na^+ doping, so that the activation energy changes accordingly, which is verified by the DFT calculations. The electrochemical model further demonstrates that the energy change is the fundamental reason for reducing the charge transfer resistance, thereby improving the reaction kinetics of Li^+. The effect of the fine microstructure changes on the electrochemical performance can be well explained in combination with the multi-scale calculation.

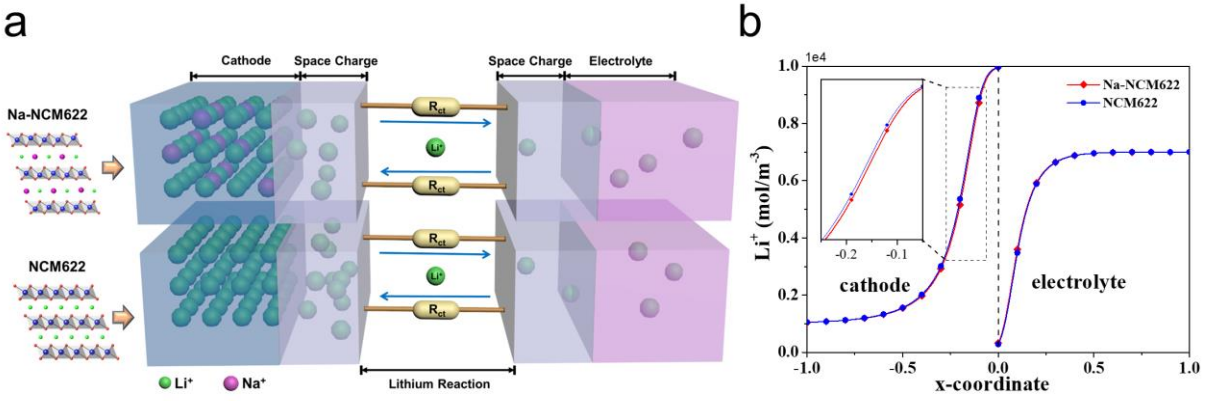

Fig. 6. (a) Schematics of the cathode/electrolyte interface, (b) the concentration distribution at the interface.

4. Conclusions

We systematically studied the Na^+ doping in a Ni-rich $LiNi_{0.6}Co_{0.2}Mn_{0.2}O_2$ (Na-NCM622) cathode material. Atomic resolution HAADF-STEM recordings with picometer precision and the corresponding intensity maps directly confirm the substitution of Na on the Li site. The results show that the introduction of Na^+ leads to a local lattice distortion and an increased interlayer spacing at the doping site. DFT calculations demonstrate that the changes of fine microstructure can reduce the activation energy barrier of materials from ΔG = 1.10 eV to ΔG = 1.05 eV, to enhance the kinetics of Li^+ diffusion. Further, the MPNP-FBV modeling methodology coupled with DFT calculations has been applied in this work to clarify the relation

between activation energy, Li^+ diffusion, charge transfer resistance and electrochemical properties. The numerical results clearly show that the charge transfer resistance can be reduced from 297 Ω to 134 Ω with a lower activation energy and faster Li^+ diffusion, which indicates an enhanced kinetics of cell reaction after Na^+-doping. As expected, the Na-NCM622 cathode exhibits a high initial Coulombic efficiency (84.40% at 4.3 V), superior cycling stability (90.8% capacity retention after 100 cycles) and rate capacities especially at high rates (105.8 mA h g^{-1} at 5 C) compared to the undoped pristine material. This work provides a direct and detailed insight into Na^+-doping materials, which is essential for establishing the relationship between the microstructure changes induced by ion doping and the electrochemical performance.

Acknowledgements

This work is supported by the National Key R&D Program of China (2016YFA0202602, 2021YFE0115800), National Natural Science Foundation of China (52103285, 22275142), Program of Introducing Talents of Discipline to Universities-Plan 111 from the Ministry of Science and Technology and the Ministry of Education of China (Grant No. B20002).

References

[1] J. Kim, H. Lee, H. Cha, M. Yoon, M. Park, J. Cho, Prospect and Reality of Ni-Rich Cathode for Commercialization, Adv. Energy Mater. 8 (2018) 1702028.

[2] W. Li, E.M. Erickson, A. Manthiram, High-nickel layered oxide cathodes for lithium-based automotive batteries, Nat. Energy 5 (2020) 26-34.

[3] M.G.S.R. Thomas, W.I.F. David, J.B. Goodenough, P. Groves, Synthesis and structural characterization of the normal spinel $LiNi_2O_4$, Mater. Res. Bull. 20 (1985) 1137-1146.

[4] M. Sathiya, A.M. Abakumov, D. Foix, G. Rousse, K. Ramesha, M. Saubanère, M.L. Doublet, H. Vezin, C.P. Laisa, A.S. Prakash, D. Gonbeau, G. VanTendeloo, J.M. Tarascon, Origin of voltage decay in high-capacity layered oxide electrodes, Nat. Mater. 14 (2015) 230-238.

[5] C. Sun, X. Liao, F. Xia, Y. Zhao, L. Zhang, S. Mu, S. Shi, Y. Li, H. Peng, G. Van Tendeloo,

K. Zhao, J. Wu, High-Voltage Cycling Induced Thermal Vulnerability in $LiCoO_2$ Cathode: Cation Loss and Oxygen Release Driven by Oxygen Vacancy Migration, ACS Nano 14 (2020) 6181-6190.

[6] D.-S. Ko, J.-H. Park, B. Yu, D. Ahn, H. Han, W. Jeon, C. Jung, A. Manthiram, Degradation of High-Nickel-Layered Oxide Cathodes from Surface to Bulk: A Comprehensive Structural, Chemical, and Electrical Analysis, Adv. Energy Mater. 10 (2020) 2001035.

[7] S.S. Zhang, Problems and their origins of Ni-rich layered oxide cathode materials, Energy Stor. Mater. 24 (2020) 247-254.

[8] W. Li, H.Y. Asl, Q. Xie, A. Manthiram, Collapse of $LiNi_{1-x-y}Co_xMn_yO_2$ Lattice at Deep Charge Irrespective of Nickel Content in Lithium-Ion Batteries, J. Am. Chem. Soc. 141 (2019) 5097-5101.

[9] C.-F. Li, K. Zhao, X. Liao, Z.-Y. Hu, L. Zhang, Y. Zhao, S. Mu, Y. Li, Y. Li, G. Van Tendeloo, C. Sun, Interface cation migration kinetics induced oxygen release heterogeneity in layered lithium cathodes, Energy Stor. Mater. 36 (2021) 115-122.

[10] W. Zou, F.-J. Xia, J.-P. Song, L. Wu, L.-D. Chen, H. Chen, Y. Liu, W.-D. Dong, S.-J. Wu, Z.-Y. Hu, J. Liu, H.-E. Wang, L.-H. Chen, Y. Li, D.-L. Peng, B.-L. Su, Probing and suppressing voltage fade of Li-rich $Li_{1.2}Ni_{0.13}Co_{0.13}Mn_{0.54}O_2$ cathode material for lithium-ion battery, Electrochim. Acta 318 (2019) 875-882.

[11] L.D. Chen, W. Zou, L. Wu, F.J. Xia, Z.Y. Hu, Y. Li, B.L. Su, Nano-Al_2O_3 Coated Li-rich Cathode Material $Li_{1.2}Ni_{0.13}Co_{0.13}Mn_{0.54}O_2$ for Highly Improved Lithium-ion Batteries, Chem J Chinese U 41 (2020) 1329-1336.

[12] H. Peng, F. Xia, C. Zhang, H. Zhuo, X. Peng, P. Song, C. Sun, J.J.A.F.M. Wu, The Coupling of Local Strain and K^+-Ion Release Induced Phase Transition Heterogeneity in Tunnel MnO_2, Adv. Funct. Mater. (2022) 2113424.

[13] J. Zhang, F. Wu, X. Dai, Y. Mai, Y. Gu, Enhancing the High-Voltage Cycling Performance

and Rate Capability of $LiNi_{0.8}Co_{0.1}Mn_{0.1}O_2$ Cathode Material by Codoping with Na and Br, ACS Sustain. Chem. Eng. 9 (2021) 1741-1753.

[14] T. Weigel, F. Schipper, E.M. Erickson, F.A. Susai, B. Markovsky, D. Aurbach, Structural and Electrochemical Aspects of $LiNi_{0.8}Co_{0.1}Mn_{0.1}O_2$ Cathode Materials Doped by Various Cations, ACS Energy Lett. 4 (2019) 508-516.

[15] R.-P. Qing, J.-L. Shi, D.-D. Xiao, X.-D. Zhang, Y.-X. Yin, Y.-B. Zhai, L. Gu, Y.-G. Guo, Enhancing the Kinetics of Li-Rich Cathode Materials through the Pinning Effects of Gradient Surface Na^+ Doping, Adv. Energy Mater. 6 (2016) 1501914.

[16] Y. Shen, X. Yao, J. Zhang, S. Wang, D. Zhang, D. Yin, L. Wang, Y. Zhang, J. Hu, Y. Cheng, X. Li, Sodium doping derived electromagnetic center of lithium layered oxide cathode materials with enhanced lithium storage, Nano Energy 94 (2022) 106900.

[17] W. He, P. Liu, B. Qu, Z. Zheng, H. Zheng, P. Deng, P. Li, S. Li, H. Huang, L. Wang, Q. Xie, D.-L. Peng, Uniform Na^+ Doping-Induced Defects in Li- and Mn-Rich Cathodes for High-Performance Lithium-Ion Batteries, Adv. Sci. 6 (2019) 1802114.

[18] A. Zh, A. Zw, B. Qj, A. Hg, A. Xl, C.J.E.A. Zy, Investigation on the effect of Na doping on structure and Li-ion kinetics of layered $LiNi_{0.6}Co_{0.2}Mn_{0.2}O_2$cathode material, Electrochim. Acta 192 (2016) 120-126.

[19] Y.-Y. Wang, Y.-Y. Sun, S. Liu, G.-R. Li, X.-P. Gao, Na-Doped $LiNi_{0.8}Co_{0.15}Al_{0.05}O_2$ with Excellent Stability of Both Capacity and Potential as Cathode Materials for Li-Ion Batteries, ACS Appl. Energy Mater. 1 (2018) 3881-3889.

[20] G. Van Tendeloo, S. Bals, S. Van Aert, J. Verbeeck, D. Van Dyck, Advanced Electron Microscopy for Advanced Materials, Adv. Mater 24 (2012) 5655-5675.

[21] Y. Lin, M. Zhou, X. Tai, H. Li, X. Han, J. Yu, Analytical transmission electron microscopy for emerging advanced materials, Matter 4 (2021) 2309-2339.

[22] X. Sang, J.M. LeBeau, Revolving scanning transmission electron microscopy: Correcting sample drift distortion without prior knowledge, Ultramicroscopy, 138 (2014) 28-35.

[23] K. Kang, G. Ceder, Factors that affect Li mobility in layered lithium transition metal oxides, Phys. Rev. B 74 (2006) 094105.

[24] Y. Liu, W.-B. Yu, B.-X. Xu, Impedance modelling of all-solid-state thin film batteries: influence of the reaction kinetics, J. Mater. Chem. A 10 (2022) 313-325.

[25] A. Vu, Y. Qian, A. Stein, Porous Electrode Materials for Lithium-Ion Batteries - How to Prepare Them and What Makes Them Special, Adv. Energy Mater. 2 (2012) 1056-1085.

[26] X. Zheng, G. Shen, C. Wang, Y. Li, D. Dunphy, T. Hasan, C.J. Brinker, B.-L. Su, Bio-inspired Murray materials for mass transfer and activity, Nat. Commun. 8 (2017) 14921.

[27] X. Tian, K. Zhou, 3D printing of cellular materials for advanced electrochemical energy storage and conversion, Nanoscale 12 (2020) 7416-7432.

[28] X. Tian, J. Jin, S. Yuan, C.K. Chua, S.B. Tor, K. Zhou, Emerging 3D-Printed Electrochemical Energy Storage Devices: A Critical Review, Adv. Energy Mater. 7 (2017) 1700127.

[29] Y. Liu, Y.-B. Ma, W. Jaegermann, R. Hausbrand, B.-X. Xu, Interface equilibrium modeling of all-solid-state lithium-ion thin film batteries, J. Power Sources 454 (2020) 227892.

[30] Y. Liu, W.-B. Yu, B.-X. Xu, New insight into the interface of TiO_2/C as nanocomposite electrode for lithium-ion batteries, J. Power Sources 534 (2022) 231406.

[31] K. Yang, L.-Z. Fan, J. Guo, X. Qu, Significant improvement of electrochemical properties of AlF_3-coated $LiNi_{0.5}Co_{0.2}Mn_{0.3}O_2$ cathode materials, Electrochim. Acta 63 (2012) 363-368.

[32] Q. Liu, X. Su, D. Lei, Y. Qin, J. Wen, F. Guo, Y.A. Wu, Y. Rong, R. Kou, X. Xiao, F. Aguesse, J. Bareño, Y. Ren, W. Lu, Y. Li, Approaching the capacity limit of lithium cobalt oxide in lithium ion batteries via lanthanum and aluminium doping, Nat. Energy 3 (2018) 936-943.

[33] K.-W. Nam, S.-M. Bak, E. Hu, X. Yu, Y. Zhou, X. Wang, L. Wu, Y. Zhu, K.-Y. Chung, X.-Q. Yang, Combining In Situ Synchrotron X-Ray Diffraction and Absorption Techniques with Transmission Electron Microscopy to Study the Origin of Thermal Instability in Overcharged Cathode Materials for Lithium-Ion Batteries, Adv. Funct. Mater. 23 (2013) 1047-1063.

[34] L. Li, L. Wang, X. Zhang, Q. Xue, L. Wei, F. Wu, R. Chen, 3D Reticular $Li_{1.2}Ni_{0.2}Mn_{0.6}O_2$ Cathode Material for Lithium-Ion Batteries, ACS Appl. Mater. Interfaces 9 (2017) 1516-1523.

[35] N.V. Kosova, V.V. Kaichev, V.I. Bukhtiyarov, D.G. Kellerman, E.T. Devyatkina, T.V. Larina, Electronic state of cobalt and oxygen ions in stoichiometric and nonstoichiometric $Li_{1+x}CoO_2$ before and after delithiation according to XPS and DRS, J. Power Sources 119-121 (2003) 669-673.

[36] S. Chong, Y. Liu, W. Yan, Y. Chen, Effect of valence states of Ni and Mn on the structural and electrochemical properties of $Li_{1.2}Ni_xMn_{0.8-x}O_2$ cathode materials for lithium-ion batteries, RSC Adv. 6 (2016) 53662-53668.

[37] T. Liu, L. Yu, J. Liu, J. Lu, X. Bi, A. Dai, M. Li, M. Li, Z. Hu, L. Ma, D. Luo, J. Zheng, T. Wu, Y. Ren, J. Wen, F. Pan, K. Amine, Understanding Co roles towards developing Co-free Ni-rich cathodes for rechargeable batteries, Nat. Energy 6 (2021) 277-286.

[38] R. Lin, S.-M. Bak, Y. Shin, R. Zhang, C. Wang, K. Kisslinger, M. Ge, X. Huang, Z. Shadike, A. Pattammattel, H. Yan, Y. Chu, J. Wu, W. Yang, M.S. Whittingham, H.L. Xin, X.-Q. Yang, Hierarchical nickel valence gradient stabilizes high-nickel content layered cathode materials, Nat. Commun. 12 (2021) 2350.

[39] O.L. Krivanek, M.F. Chisholm, V. Nicolosi, T.J. Pennycook, G.J. Corbin, N. Dellby, M.F. Murfitt, C.S. Own, Z.S. Szilagyi, M.P. Oxley, S.T. Pantelides, S.J. Pennycook, Atom-by-atom structural and chemical analysis by annular dark-field electron microscopy, Nature 464 (2010) 571-574.

[40] Q. Zhang, L.Y. Zhang, C.H. Jin, Y.M. Wang, F. Lin, CalAtom: A software for quantitatively analysing atomic columns in a transmission electron microscope image, Ultramicroscopy 202 (2019) 114-120.

[41] J.H. Jang, Y.-M. Kim, Q. He, R. Mishra, L. Qiao, M.D. Biegalski, A.R. Lupini, S.T. Pantelides, S.J. Pennycook, S.V. Kalinin, A.Y. Borisevich, In Situ Observation of Oxygen

Vacancy Dynamics and Ordering in the Epitaxial $LaCoO_3$ System, ACS Nano 11 (2017) 6942-6949.

[42] S. Liu, Z. Dang, D. Liu, C. Zhang, T. Huang, A. Yu, Comparative studies of zirconium doping and coating on $LiNi_{0.6}Co_{0.2}Mn_{0.2}O_2$ cathode material at elevated temperatures, J. Power Sources 396 (2018) 288-296.

[43] Q. Ma, Z. Chen, S. Zhong, J. Meng, F. Lai, Z. Li, C. Cheng, L. Zhang, T. Liu, Na-substitution induced oxygen vacancy achieving high transition metal capacity in commercial Li-rich cathode, Nano Energy 81 (2021) 105622.

[44] L. Zou, W. Zhao, Z. Liu, H. Jia, J. Zheng, G. Wang, Y. Yang, J.-G. Zhang, C. Wang, Revealing Cycling Rate-Dependent Structure Evolution in Ni-Rich Layered Cathode Materials, ACS Energy Lett. 3 (2018) 2433-2440.

[45] C. Hong, Q. Leng, J. Zhu, S. Zheng, H. He, Y. Li, R. Liu, J. Wan, Y. Yang, Revealing the correlation between structural evolution and Li^+ diffusion kinetics of nickel-rich cathode materials in Li-ion batteries, J. Mater. Chem. A 8 (2020) 8540-8547.

[46] K.C. Mahesh, G.S. Suresh, T.V. Venkatesha, Electrochemical behavior of $Li[Li_{0.2}Co_{0.3}Mn_{0.5}]O_2$ as cathode material in Li_2SO_4 aqueous electrolyte, J. Solid State Electrochem. 16 (2012) 3559-3571.

[47] J. Tian, Y. Su, F. Wu, S. Xu, F. Chen, R. Chen, Q. Li, J. Li, F. Sun, S. Chen, High-Rate and Cycling-Stable Nickel-Rich Cathode Materials with Enhanced Li^+ Diffusion Pathway, ACS Appl. Mater. Interfaces 8 (2016) 582-587.

[48] J.W. Kim, D.H. Kim, D.Y. Oh, H. Lee, J.H. Kim, J.H. Lee, Y.S. Jung, Surface chemistry of $LiNi_{0.5}Mn_{1.5}O_4$ particles coated by Al_2O3 using atomic layer deposition for lithium-ion batteries, J. Power Sources 274 (2015) 1254-1262.

[49] J. Zhu, Z. Sun, X. Wei, H. Dai, Studies on the medium-frequency impedance arc for Lithium-ion batteries considering various alternating current amplitudes, J Appl Electrochem 46 (2016) 157-167.

[50] S.S. Zhang, K. Xu, T.R. Jow, Electrochemical impedance study on the low temperature of Li-ion batteries, Electrochim. Acta 49 (2004) 1057-1061.

[51] Y. Wei, J. Zheng, S. Cui, X. Song, Y. Su, W. Deng, Z. Wu, X. Wang, W. Wang, M. Rao, Y. Lin, C. Wang, K. Amine, F. Pan, Kinetics Tuning of Li-Ion Diffusion in Layered $Li(Ni_xMn_yCo_z)O_2$, J. Am. Chem. Soc 137 (2015) 8364-8367.

[52] B. Chu, L. You, G. Li, T. Huang, A. Yu, Revealing the Role of W-Doping in Enhancing the Electrochemical Performance of the $LiNi_{0.6}Co_{0.2}Mn_{0.2}O_2$ Cathode at 4.5 V, ACS Appl. Mater. Interfaces 13 (2021) 7308-7316.

[53] T. Nishida, K. Nishikawa, Y. Fukunaka, Diffusivity Measurement of $LiPF_6$, LiTFSI, $LiBF_4$ in PC, ECS Trans 6 (2008) 1-14.